

Boosting Nitrogen Reduction to Ammonia on FeN₄ Sites by Atomic Spin Regulation

Yajin Wang, Wenzheng Cheng, Pengfei Yuan, Gege Yang, Shichun Mu, Jialin Liang, Huicong Xia, Kai Guo, Mengli Liu, Shuyan Zhao, Gan Qu, Bang-An Lu, Yongfeng Hu, Jinsong Hu, and Jia-Nan Zhang*

Understanding the relationship between the electronic state of active sites and N₂ reduction reaction (NRR) performance is essential to explore efficient electrocatalysts. Herein, atomically dispersed Fe and Mo sites are designed and achieved in the form of well-defined FeN₄ and MoN₄ coordination in polyphthalocyanine (PPc) organic framework to investigate the influence of the spin state of FeN₄ on NRR behavior. The neighboring MoN₄ can regulate the spin state of Fe center in FeN₄ from high-spin ($d_{xy}^2 d_{yz}^1 d_{xz}^1 d_{z^2}^1 d_{x^2-y^2}^1$) to medium-spin ($d_{xy}^2 d_{yz}^2 d_{xz}^1 d_{z^2}^1$), where the empty d orbitals and separate d electron favor the overlap of Fe 3d with the N 2p orbitals, more effectively activating N≡N triple bond. Theoretical modeling suggests that the NRR preferably takes place on FeN₄ instead of MoN₄, and the transition of Fe spin state significantly lowers the energy barrier of the potential determining step, which is conducive to the first hydrogenation of N₂. As a result, FeMoPPc with medium-spin FeN₄ exhibits 2.0 and 9.0 times higher Faradaic efficiency and 2.0 and 17.2 times higher NH₃ yields for NRR than FePPc with high-spin FeN₄ and MoPPc with MoN₄, respectively. These new insights may open up opportunities for exploiting efficient NRR electrocatalysts by atomically regulating the spin state of metal centers.

1. Introduction

As an important precursor to fertilizers in daily life, ammonia (NH₃) is essential for agriculture and industry.^[1–4] Nowadays, industrial synthesis of NH₃ using N₂ and H₂ relies on the Haber–Bosch process at high temperatures (400–600 °C) and high pressure (20–40 MPa) which consumes a large amount of energy with emission of CO₂.^[5–11] Among the alternative methods,^[12–14] the electrocatalytic N₂ reduction reaction (NRR) using water as hydrogen source under ambient conditions has been considered as sustainable artificial N₂ fixation to produce NH₃.^[15–19] However, the following challenges remains for the NH₃ production via NRR: a) the adsorption and activation of N₂ on the catalytic sites and the difficulties in breaking strong N≡N triple bond, leading to the very low NH₃ yield;^[20–22] b) the competing hydrogen evolution reaction (HER) in aqueous electrolytes, resulting in the low Faradaic efficiency (FE).^[23–25] Therefore, understanding the structure–activity

Y. Wang, W. Cheng, G. Yang, J. Liang, H. Xia, K. Guo, M. Liu, S. Zhao, G. Qu, B.-A. Lu, J.-N. Zhang
College of Materials Science and Engineering
Zhengzhou University
Zhengzhou 450001, P. R. China
E-mail: zjn@zzu.edu.cn

P. Yuan
International Joint Research Laboratory for Quantum Functional Materials of Henan Province and School of Physics and Microelectronics
Zhengzhou University
Zhengzhou 450001, P. R. China

S. Mu
State Key Laboratory of Advanced Technology for Materials Synthesis and Processing
Wuhan University of Technology
Wuhan 430070, P. R. China

S. Mu
Foshan Xianhu Laboratory of the Advanced Energy Science and Technology Guangdong Laboratory
Xianhu Hydrogen Valley
Foshan 528200, China

Y. Hu
Canadian Light Source
44 Innovation Boulevard Saskatoon, Saskatoon, SK S7N 2V3, Canada

J. Hu
Beijing National Laboratory for Molecular Sciences (BNLMS)
CAS Key Laboratory of Molecular Nanostructure and Nanotechnology
Institute of Chemistry
Chinese Academy of Sciences
Beijing 100190, China

 The ORCID identification number(s) for the author(s) of this article can be found under <https://doi.org/10.1002/advs.202102915>

© 2021 The Authors. Advanced Science published by Wiley-VCH GmbH. This is an open access article under the terms of the Creative Commons Attribution License, which permits use, distribution and reproduction in any medium, provided the original work is properly cited.

DOI: 10.1002/advs.202102915

relationship of catalytic sites for NRR is critical to the exploration of efficient electrocatalysts for feasible industrial NH_3 production from inert N_2 via NRR. To date, various materials, including noble-metal-based,^[26] non-noble metal-based,^[27] metal-free,^[28] and single atomic materials,^[29,30] have been investigated as electrocatalysts for NRR. Among them, single atom catalysts with the maximum of atom utilization exhibit remarkably enhanced catalytic activity and selectivity.^[31,32]

As one of the most earth-abundant elements, Fe-based materials have been given increasing attention as NRR catalysts.^[27,33] According to the theoretical prediction, Mo-based catalysts are also promising candidates for N_2 activation.^[34–36] Moreover, it is notable that the long-range coupling of hetero-single-atom (h-SAs) can be used to change the electronic structure of active site and enhance its catalytic performance. Zhao et al.^[37] reported that the atomically dispersed FeN_4 and NiN_4 coanchored on a microsized N-doped graphitic carbon exhibited the enhanced performance for oxygen reduction reaction (ORR) through the synergetic effect. It implies that harnessing the synergy from h-SAs would be effective for the design of NRR catalysts although the underlying mechanism for such enhancement still remains unclear.

Recent studies have reported that the electronic structure of catalytic sites can be tuned by changing the spin state of transition metals, offering the possibility for enhancing the catalytic performance. Due to the unique coordination environment, Fe possesses multiple spin states, i.e., low-spin, medium-spin, and high-spin states. The Fe in the low-spin state (no electron filling in the e_g orbital) has no singlet electron to pair with the intermediate.^[38] The Fe in the high-spin state (e_g filled with two single electrons) usually displays excessive orbital overlap with the intermediates that limits the desorption of reaction product,^[39] resulting in inferior catalytic performance. In contrast, the Fe in the medium-spin state (e_g filled with a singlet electron) can readily interact with reaction intermediates via σ -bonding.^[40]

Zhao and co-workers^[39] suggested that the coexistence of Fe 3d itinerant charge and medium-spin polarization induced by the spin-state change of Fe in the Fe–NFe–Ni atomic pair contributed to its excellent bifunctional electrocatalytic activity for both ORR and OER. We recently found that the Mn–N could effectively activate Fe^{III} center for ORR by changing its spin state in the dual-metal atomically dispersed Fe,Mn/N–C catalyst.^[38] However, the electronic configurations of ground-state O_2 and N_2 molecules are completely different according to the molecular orbital theory. O_2 has a spin-triplet state with two unpaired electrons, while N_2 is diamagnetic with all electrons paired up.^[28] Thus, the spin regulation and its influence on NRR performance would be significantly different from ORR/OER, which have been not investigated and revealed yet although it might be an efficient strategy to accelerate the NRR kinetics.

To fill puzzle, we herein designed and successfully fabricated a well-defined Fe–Mo h-SA NRR electrocatalyst with atomically dispersed FeN_4 and MoN_4 coordination sites coanchored in polyphthalocyanine organic framework (FeMoPPc) by a low-temperature melt polymerization. Density functional theory (DFT) calculation and experimental results reveal that the introduction of Mo SAs induced the charge accumulation on the Fe active sites, which promotes the adsorption and activation of N_2 .

Importantly, the change of Fe spin state from high to medium spin simultaneously facilitated the potential determining step (PDS) of NRR, the first protonation step. Due to the synergistic effect of charge accumulation and spin redistribution, the difficulties in activating $\text{N}\equiv\text{N}$ triple bond and protonation hydrogenation were effectively mitigated. As a result, the obtained FeMoPPc with medium-spin Fe center exhibited 2.0 and 9.0 times higher Faradic efficiencies and 2.0 and 17.2 times higher NH_3 yields for NRR than FePPc with high-spin Fe and MoPPc with Mo active center, respectively.

2. Results and Discussion

As illustrated in **Figure 1a**, FeMoPPc was synthesized by a low-temperature solvent-free solid-phase polymerization of pyromellitic dianhydride, urea, FeCl_3 , and MoCl_3 with the $(\text{NH}_4)_2\text{Mo}_2\text{O}_7$ as initiator (see the details in the Supporting Information). Typically, pyromellitic dianhydride and urea were employed as organic phthalocyanine precursor and metal chlorides were used as metal source, respectively. The above chemicals were first mixed and ground uniformly in an agate mortar, and then heated at 220 °C for 3 h for polymerization process. Specifically, the anhydrides group in the pyromellitic dianhydride reacts with the amino group of urea to form the imide group, which continues to react with the amino group of urea and give the iminoisoindoline. Meanwhile, Fe ions and Mo ions were coordinated with the amino groups of iminoisoindoline monomer and subsequently form phthalocyanine network polymer containing $\text{Fe}(\text{Mo})\text{N}_4$.^[41–43] The proper diameter of the ring cavity in the polyphthalocyanine structure can accommodate Fe and Mo metal atoms, forming a metal phthalocyanine coordination polymer with homogeneous distributions of Fe and Mo. The control samples FePPc and MoPPc were prepared in parallel excepting for using Fe or Mo source alone instead of both for FeMoPPc.

Field-emission scanning electron microscopy (SEM) and transmission electron microscopy (TEM) images of FeMoPPc (**Figure S1a,b**, Supporting Information) show a fluffy porous morphology,^[41] similar to that of KB (**Figure S2**, Supporting Information). No metal-based particles or aggregations were observed in the TEM image (**Figure S1c**, Supporting Information), indicating the uniform loading of FeMoPPc on the substrate. The high-resolution TEM (HR-TEM) image (**Figure S1d**, Supporting Information) and the corresponding selected area electron diffraction (SAED) image (inset in **Figure S1d** in the Supporting Information) demonstrate the amorphous structure for FeMoPPc. Field-emission scanning electron microscopy energy dispersive spectroscopic (SEM-EDS) elemental mapping displays C, N, Fe, and Mo are uniformly distributed, indicating that FeMoPPc is evenly loaded on carbon substrate (**Figure S3**, Supporting Information). This result is consistent with X-ray diffraction (XRD) measurements (**Figure S4**, Supporting Information), indicating the absence of the long-range order in FeMoPPc. Some individual bright points can be observed in the high-angle annular dark-field scanning TEM (HAADF-STEM) images (**Figure 1b,c**), suggesting that Fe and Mo should exist in the form of single atoms in FeMoPPc. EDS elemental mapping displays the homogeneous distribution of C, N, Fe, and Mo elements (**Figure 1d**). The FT-IR spectra (**Figure 1e**) of FePPc, FeMoPPc, and MoPPc show obvious phthalocyanine skeletal vibration in

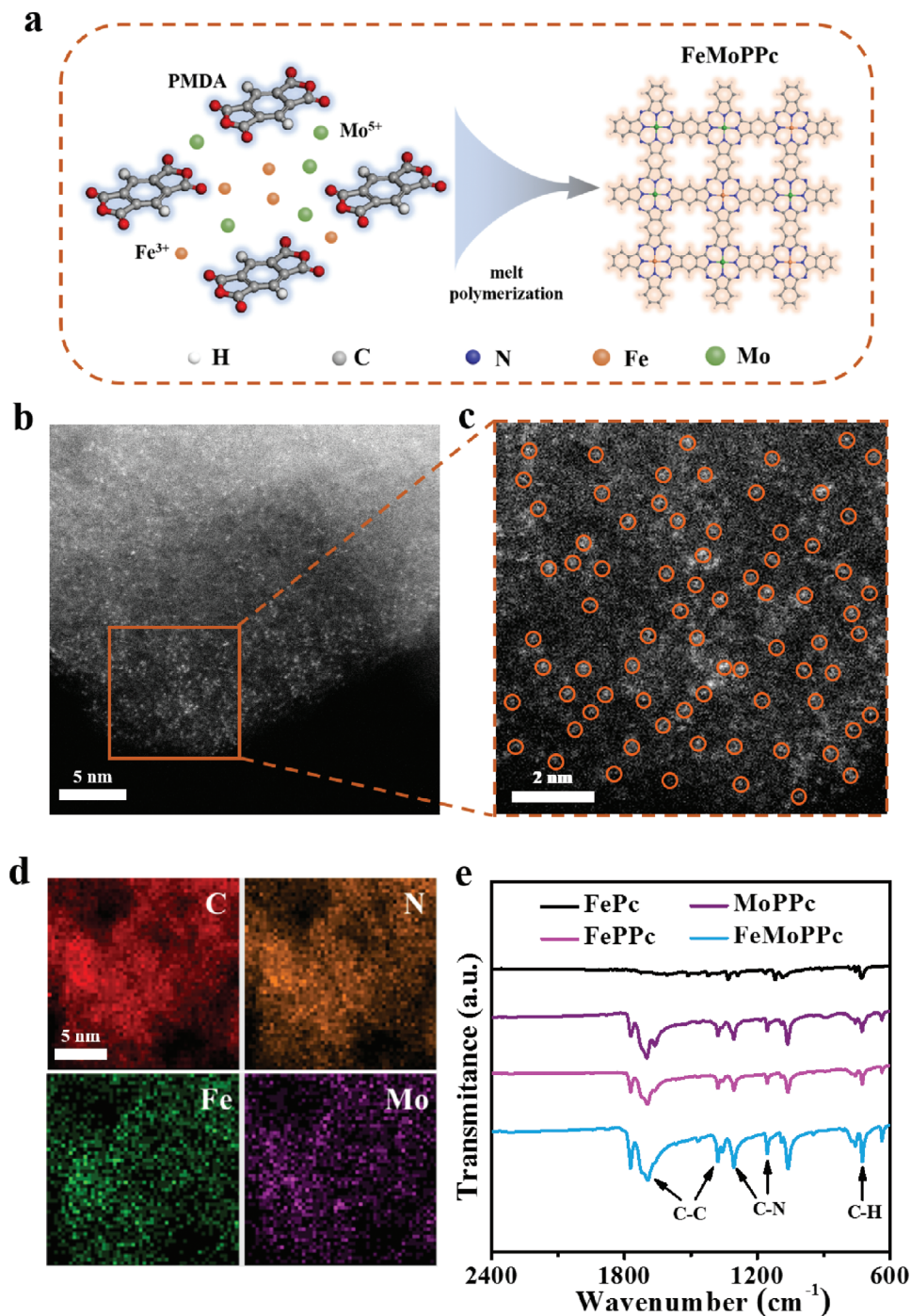


Figure 1. Synthetic illustration, TEM, and IR characterizations of FeMoPPc catalyst. a) Synthetic procedure of FeMoPPc. b) HAADF-STEM image of FeMoPPc. c) Enlarged view of selected area HAADF-STEM image of FeMoPPc. d) EDS elemental mapping of C, N, Fe, and Mo in FeMoPPc. e) FTIR spectra of FePc, FePPc, MoPPc, and FeMoPPc.

the range of 700–1600 cm^{-1} ,^[8] and these results suggest the successful formation of metal polyphthalocyanine frameworks. The Brunauer–Emmett–Teller (BET) specific surface area of FeMoPPc on KB is much lower than that of KB itself ($63.3 \text{ cm}^2 \text{ g}^{-1}$ vs $1347.2 \text{ cm}^2 \text{ g}^{-1}$) (Figure S5, Supporting Information), further evidencing the successful loading of FeMoPPc on KB.

The chemical states and coordination environment of Fe and Mo atoms in FeMoPPc were further determined by X-ray photoelectron spectroscopy (XPS) and X-ray absorption spectroscopy (XAS). XPS spectrum of FeMoPPc confirms the presence of Fe, Mo, C, and N elements (Figure S6a, Supporting Information). The high-resolution Fe 2p XPS exhibits two peaks at 709.7 and

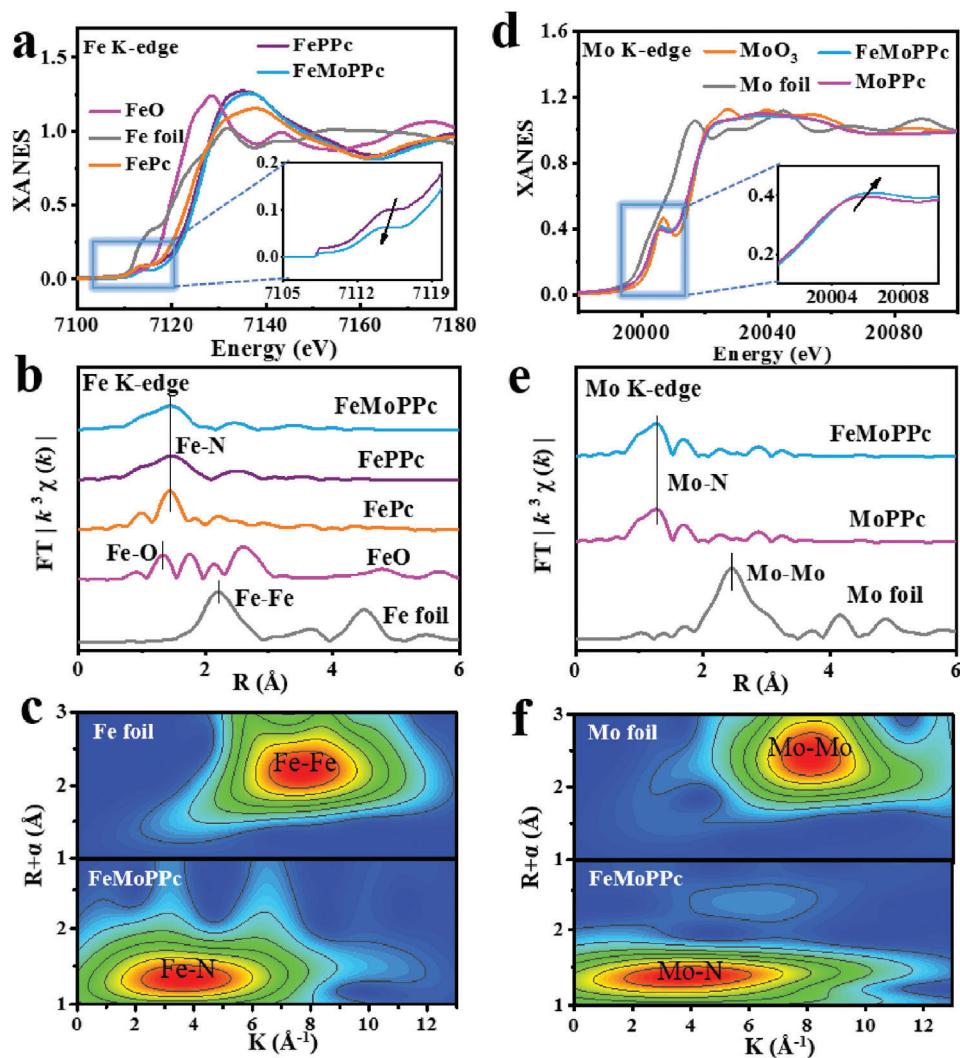


Figure 2. XAS spectrum of the catalysts. a) Fe K-edge XANES and b) Fourier-transformed for the catalyst FeMoPPc and other standard samples. c) Wavelet transform of Fourier-transformed EXAFS data of Fe foil, FeMoPPc. d) Mo K-edge XANES and e) Fourier-transformed for the catalyst FeMoPPc and other standard samples. R is the distance in Ångströms ($1 \text{ \AA} = 10^{-10} \text{ m}$); k is the wave number. f) Wavelet transform of Fourier-transformed EXAFS data of Mo foil, FeMoPPc.

722.2 eV (Figure S6b, Supporting Information), corresponding to Fe $2p_{3/2}$ and Fe $2p_{1/2}$, respectively. The estimated valence state of Fe is +2.^[44] There are two shakeup satellites peaks (denoted as “Sat.”) centered at 709.7 and 722.2 eV. In Mo 3d XPS (Figure S6c, Supporting Information), the split peaks centered at 230.4 and 233.5 eV can be assigned to the Mo $3d_{5/2}$ and Mo $3d_{3/2}$ of Mo^{4+} ,^[45] respectively. The N 1s XPS (Figure S6d, Supporting Information) reveals the coexistence of five types of N species for FeMoPPc, including oxidized N (402.6 eV), pyrrolic N (400.8 eV), Fe–N (399.8 eV), pyridinic N (398.5 eV), and Mo–N (397.4 eV).^[46] The content of Fe and Mo detected by inductively coupled plasma atomic emission spectroscopy (ICP-AES) analysis are 1.28 and 5.83 wt%, respectively (see Table S1 in the Supporting Information for more details).

The normalized Fe K-edge X-ray absorption near edge structure (XANES) spectra display that the Fe states of FeMoPPc and FePPc are similar to that of FePc (Figure 2a).^[47,48] It is worth not-

ing that the absorption edge of FeMoPPc shifts slightly to the lower energy compared to that of FePPc (inset in Figure 2a), indicating that the introduction of Mo has an effect on the coordination environment of Fe. In reference to FeO and Fe foil, the Fourier-transformed extended X-ray absorption fine structure (FT-EXAFS) spectra of the FeMoPPc shows a main peak at 1.4 Å belonging to the Fe–N scattering paths while no Fe–Fe interaction peak located at $>2.2 \text{ \AA}$ and Fe–O peak at 1.2 Å were observed (Figure 2b), confirming the atomic dispersion of Fe in FeMoPPc. Wavelet transforms of Fe K-edge EXAFS oscillations were performed to further investigate the status of Fe atoms. WT analysis of FeMoPPc spectrum shows only one intensity maximum at about 4.0 \AA^{-1} (Figure 2c), very similar to the reference FePc (at $\approx 4.0 \text{ \AA}^{-1}$) (Figure S7a, Supporting Information) but distinct from the Fe foil (at $\approx 7.5 \text{ \AA}^{-1}$). These results suggest that FeMoPPc has the FeN_4 structure like that in FePc. Using this structural model, all the fitted Fe K-edge EXAFS in R space (blue line) and k space

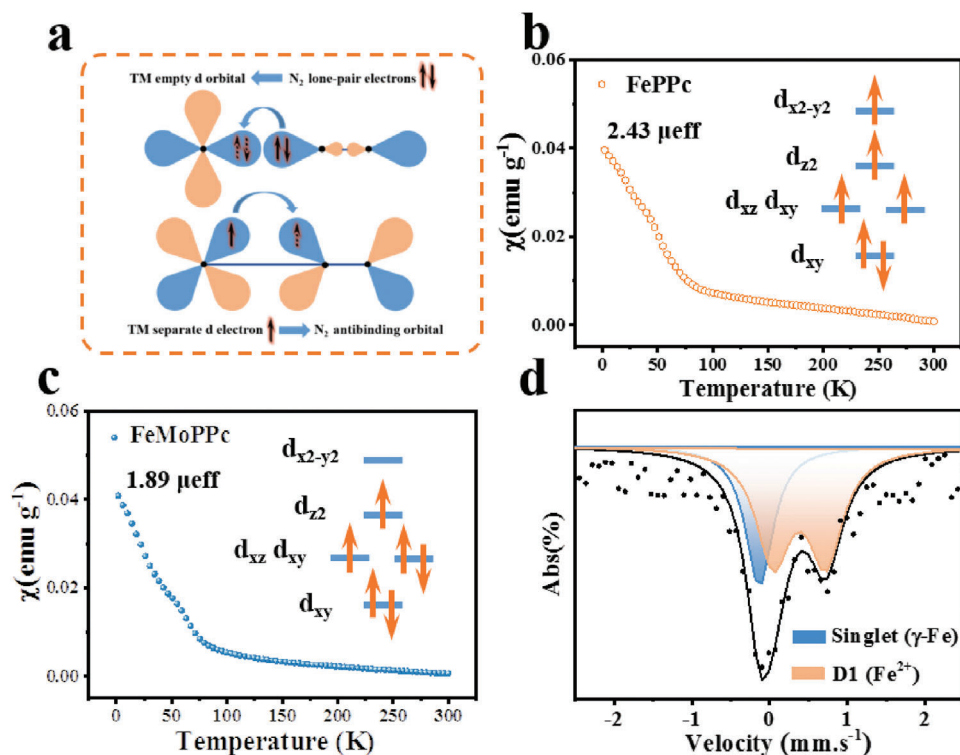


Figure 3. Magnetic susceptibility and ^{57}Fe Mössbauer spectroscopy of the catalysts. a) Simplified schematic of N_2 bonding to transition metals. b,c) Magnetic susceptibility of b) FePPc and c) FeMoPPc. d) Room-temperature ^{57}Fe Mössbauer spectrum of FeMoPPc. The data (scattered dots) are shown with the best fit (black dash line) and the deconvolutions of two components as indicated by the legend.

(blue line) match well with the experimental data (red circles) (Figure S7b,c, Supporting Information). The fitting results show that the isolated Fe atom coordinates with N atoms in an average coordination number of 4 and an average Fe–N bond length is 1.96 Å (see Table S2 in the Supporting Information for more details). Meanwhile, two O atoms are adsorbed on the Fe atom in side-on mode, which is well compatible with WT.

Moreover, the Mo K-edge XANES spectra display that FeMoPPc and MoPPc have similar Mo edge feature (Figure 2d), indicating the chemical environment of Mo–N coordination.^[29] In the FT-EXAFS spectra (Figure 2e), FeMoPPc shows a main peak belonging to the Mo–N scattering paths located at 1.3 Å while no Mo–Mo peak is detected at about 2.5 Å,^[29] confirming the atomic dispersion of Mo. WT analyses of Mo K-edge EXAFS oscillations corroborate that Mo exists in the form of single atomic Mo–N in FeMoPPc in view of one intensity maximum at about 4.0 Å⁻¹ (Figure 2f; Figure S8a, Supporting Information) which is distinct from the feature of Mo foil (≈ 8.0 Å⁻¹). All the fitted Mo K-edge EXAFS in R space (blue line) and k space fitting curve (blue line) support the proposed atomic Mo–N coordination structure (Figure S8b,c, Supporting Information). The average coordination number is around 4 and an average Mo–N bond length is ≈ 1.76 Å (Table S2, Supporting Information).

Theoretically, the NRR performance on a transition metal (TM)-based catalyst is related to the occupancy rate of its d orbitals.^[49] On the one hand, metal center should have empty d orbitals to accept the lone-pair electrons of N_2 . On the other hand, the separate d electron is expected to contribute to the anti-

bonding orbital of N_2 , weakening the strong $\text{N}\equiv\text{N}$ triple bond (π -backdonation) (Figure 3a).^[50] In this regard, the zero-field cooling (ZFC) temperature-dependent magnetic susceptibility measurements were carried out to reveal the electronic configuration of the d orbitals of Fe in FeMoPPc. Figure 3b,c shows a nearly temperature-independent paramagnetism for both FePPc and FeMoPPc. Notably, the calculated effective magnetic moment^[38] of Fe sites for adsorption goes from 2.43 to 1.89 μ_{eff} after the introduction of Mo. Moreover, the density of states (DOS) of FeMoPPc undergoes partial spin splitting compared with FePPc, indicating that the spin state of Fe species in FeMoPPc is reduced (Figure S9, Supporting Information).^[51] It suggests that Fe center changes from high spin ($d_{xy}^2 d_{yz}^1 d_{xz}^1 d_{z^2}^1 d_{x^2-y^2}^1$) to medium spin ($d_{xy}^2 d_{yz}^2 d_{xz}^1 d_{z^2}^1$) after adding Mo, where it has both empty d orbitals and separate d electron.^[52,53] Such Fe 3d orbitals would effectively overlap with the N 2p orbital while weakening the $\text{N}\equiv\text{N}$ triple bond.

^{57}Fe Mössbauer spectroscopy of FeMoPPc was further recorded to analyze the Fe state. As shown in Figure 3d, a singlet and a doublet (D1) can be fitted. The singlet state is usually assigned to $\gamma\text{-Fe}$. With the largest quadrupole splitting (QS) value, D1 can be assigned to FePc-like medium-spin $\text{Fe}^{\text{II}}\text{N}_4$ species.^[48] The quantitative analysis shows that the content of D1 is 66.3% (Table S3, Supporting Information), indicating that Fe^{II} mainly exists in medium spin in FeMoPPc. Otherwise, if Fe is in high spin where two unpaired electrons sit in e_g orbital, Fe 3d and N 2p orbital will excessively overlap, resulting in too strong interaction and difficulty in the first hydrogenation step. Based the

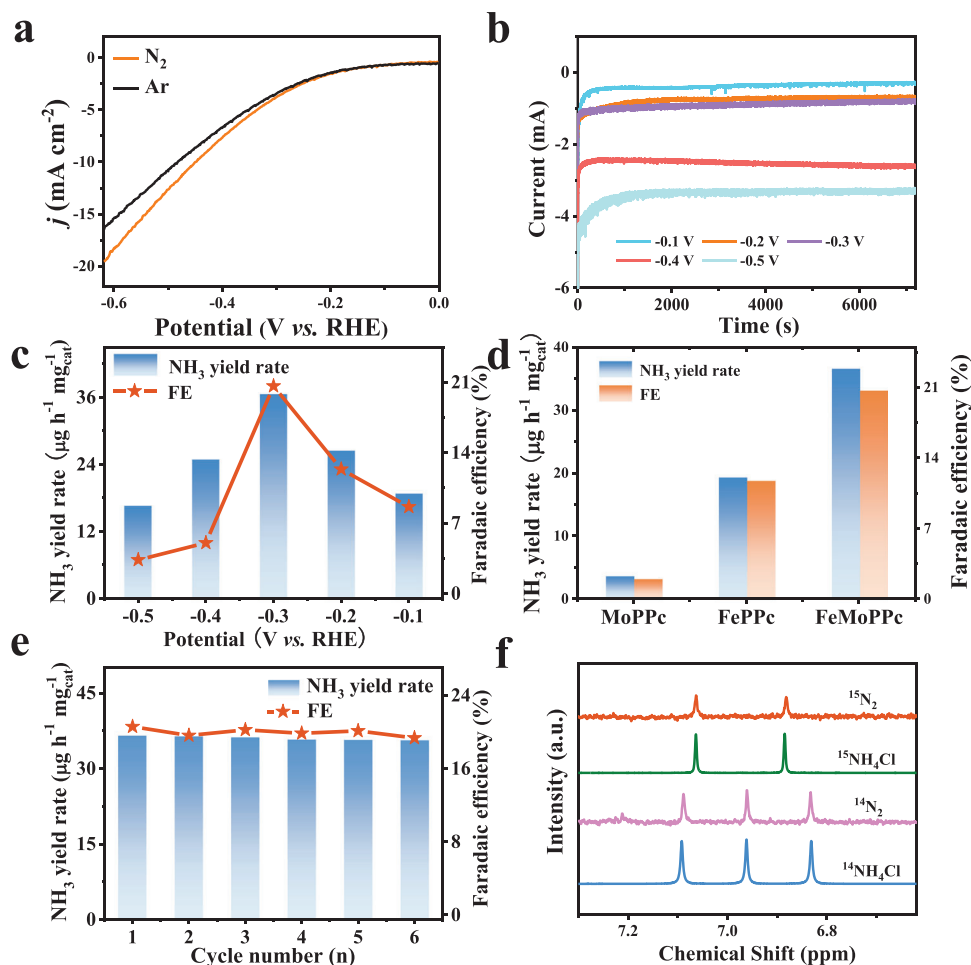


Figure 4. NRR electrochemical performances of FeMoPPc in 0.1 M KOH. a) Linear sweep voltammetry curves in N₂ (orange line) and Ar-saturated (black line) KOH solutions. b) Chronoamperometry results at different potentials. c) NH₃ yield rate and Faradaic efficiency at the corresponding potentials. d) NH₃ yield rate and Faradaic efficiency of MoPPc, FePPc, and FeMoPPc in N₂-saturated 0.1 M KOH solution at -0.3 V for 2 h, respectively. e) Cycling test of FeMoPPc for the NRR at -0.3 V. f) ¹H NMR analysis of the electrolyte fed by ¹⁴N₂ and ¹⁵N₂ after the electrolytic reaction.

above data, the neighboring MoN₄ sites appreciably regulates the spin state of Fe center from high spin to medium spin, promoting π -backdonation process and the first hydrogenation of N₂, as discussed later.

Inspiring by this change in spin state and motivation of revealing its effects on the electrocatalytic NRR performance, we systematically evaluated the catalytic performances of FeMoPPc, FePPc, and MoPPc for NRR in an H-type cell (Figure S10, Supporting Information) using N₂ or Ar-saturated 0.1 M KOH solution as the electrolyte.^[54] All the potentials hereinafter were referred to the reversible hydrogen electrode (RHE). As shown in **Figure 4a**, an obvious shift in the linear sweep voltammetry (LSV) curves was detected for FeMoPPc when switching the electrolyte from Ar-saturated solution to N₂-saturated one, implying its possible activity for NRR. Figure S11 in the Supporting Information shows the LSV curves of the FePPc and MoPPc and N₂-saturated 0.1 M KOH solution. The yields of NH₃ were evaluated by the indophenol blue method using NH₄Cl solutions as standards.^[26] As shown in Figure S12 (Supporting Information), under alkaline conditions, the absorbance of standard solutions in various

concentrations can be recorded at a wavelength of 655 nm. The fitting curves give excellent linear correlations of absorbances with NH₄Cl concentrations under both alkaline and acidic electrolytes (Figure S13, Supporting Information), enabling the reliable determination of NH₃ yields for NRR experiments.

During the synthetic process, the atomic ratio of Fe to Mo in FeMoPPc was adjusted by simply changing the amounts of source FeCl₃ and MoCl₅. XPS was carried out to analyze the atomic ratios of Fe to Mo in the samples (Table S4, Supporting Information). For example, 0.5:1 of FeCl₃:MoCl₅ gives $\approx 0.71:1$ of Fe/Mo in FeMoPPc. Electrochemical NRR tests were then performed on a series of FeMoPPc samples with different Fe:Mo ratios. It was found that when using 0.5:1 of FeCl₃:MoCl₅ the NH₃ yield and FE on FeMoPPc are the highest (Figure S14, Supporting Information). The chronoamperometric curves were collected over 2 h under various testing potentials ranging from -0.1 to -0.5 V, and the NRR measurements demonstrate that NH₃ yield and FE on FeMoPPc reach the highest values of 36.33 $\mu\text{g h}^{-1} \text{mg}_{\text{cat}}^{-1}$ and 20.62% at -0.3 V, respectively (Figure 4b,c; Figure S15, Supporting Information). Compared with

the previous reports, such performance ranks top tier among Fe-based or Mo-based catalysts (Figure S16 and Table S5, Supporting Information). More impressively, these values are 2.0 times higher than those on FePPc where the Fe center is in medium spin instead of high spin (Figure 4d), suggesting the spin state of Fe center significantly affects the NH_3 yield and FE. Moreover, it is worth noting that NH_3 yield and FE on FeMoPPc are 9.0 and 17.2 times higher than those on MoPPc with only MoN_4 sites (Figure 4d), implying the FeN_4 sites may be much more active than MoN_4 for NRR. The cycling tests were further performed to probe the durability. As shown in Figure 4e, no obvious variation for the NH_3 yields and FE in successive six cycling is observed. Furthermore, the FeMoPPc working electrode outputs stable current densities of NRR in this cycling tests (Figure S17, Supporting Information). All these results corroborate the superior durability of FeMoPPc for NRR.

Subsequently, the method of Watt and Chrisp^[26] was used to probe the possible by-product hydrazine (N_2H_4) in the electrolyte. As shown in Figure S18 (Supporting Information), a series of standard N_2H_4 solutions with different concentrations were used to plot the calibration curves of N_2H_4 in KOH solutions and HCl solutions (Figure S19, Supporting Information), respectively. The testing results prove that no N_2H_4 was produced in the system (Figure S20, Supporting Information), indicating that FeMoPPc has excellent selectivity to NH_3 production via NRR.

To reveal if the detected NH_3 is truly produced by electrocatalytic conversion of N_2 flowed into the electrolytic cell rather than from possible contaminations (such as gas source, human breath, electrolyte, and environment, etc.), a series of control experiments were carried out. As shown in Figures S21 and S22 (Supporting Information), negligible NH_3 were detected for the control experiments with a bare carbon paper with the N_2 -saturated electrolyte (carbon paper- N_2), FeMoPPc with the Ar-saturated electrolyte (FeMoPPc-Ar), open circuit or a KOH background at -0.3 V. This suggests that the NH_3 was generated from electroreduction of supplied N_2 by FeMoPPc catalyst. To give an unambiguous conclusion, isotopic labeling experiments were further performed and confirmed that the N in NH_3 product originated from the supplied N_2 . As indicated by the ^1H nuclear magnetic resonance (NMR) spectra (Figure 4f), triplet coupling for $^{14}\text{NH}_4^+$ and doublet coupling for $^{15}\text{NH}_4^+$ were clearly detected when $^{14}\text{N}_2$ and $^{15}\text{N}_2$ were bubbled over the cathode, respectively. These signals are in well consistence with those recorded with standard solutions of $^{14}\text{NH}_4\text{Cl}$ and $^{15}\text{NH}_4\text{Cl}$. These results reliably suggest that the detected NH_3 is truly from NRR on FeMoPPc.

DFT calculations were subsequently performed to unveil the underlying mechanism of the overall NRR on such bimetallic Fe–Mo h-SAs coanchored in polyphthalocyanine organic framework. Specific DFT calculation information and constant settings (Table S6, Supporting Information) can be seen in Supporting Information. According to experimental results, FeN_4 and MoN_4 sites were proposed as the structural models (Figure S23, Supporting Information). Figure 5a shows the calculated Gibbs free energy diagrams for NRR on FeN_4 and MoN_4 sites in FeMoPPc via the alternating pathways (Figure S24, Supporting Information). It is seen that the first hydrogenation process ($^*\text{N}_2 \rightarrow ^*\text{NNH}$) appears to be the PDS for FeN_4 site with an energy barrier of 0.66 eV. In contrast, The PDS on MoN_4 site is the second hydrogenation

process ($^*\text{NNH} \rightarrow ^*\text{NHNH}_2$) with an energy barrier of 0.83 eV (Figure 5a; Figure S25, Supporting Information). Moreover, the desorption of NH_3 on FeN_4 site only needs to overcome a small energy barrier of 0.09 eV while that on MoN_4 site shows a much higher energy barrier (0.54 eV). These results suggest that FeN_4 site is more active than MoN_4 site in FeMoPPc for NRR, rationalizing the fact that FeMoPPc exhibits 9.0 times higher FE and 17.2 times higher NH_3 yields for NRR than MoPPc with MoN_4 sites only. As shown in Figure S26 (Supporting Information), the DFT calculation of FeN_4 site in FePPc has been performed. The PDS on FeN_4 site is 1.42 eV, which is larger than FeN_4 site of FeMoPPc, indicating that the addition of Mo promotes the NRR process on FeN_4 site. In view of the Fe spin-state analysis, it might be ascribed to the fact that the introduction of MoN_4 moieties causes the transition of Fe spin state from high spin ($d_{xy}^2 d_{yz}^1 d_{xz}^1 d_{z^2}^1 d_{x^2-y^2}^1$) to medium spin ($d_{xy}^2 d_{yz}^2 d_{xz}^1 d_{z^2}^1$). Moreover, the projected density of states (PDOS) results shows that the d-band center of Fe/FeMoPPc occurs positive shift compared to Fe/FePPc,^[55] indicating that it is easier to adsorb N_2 and coincide with N p orbital (Figure S27, Supporting Information).

HER is known to be the main competitive reaction against NRR. Therefore, the HER activity of the two active sites was also investigated. For dual component active sites of FeMoPPc, one with $\Delta G_{\text{H}} < 0$ ($\Delta G_{\text{H-negative}}$, strong H adsorption) and another one with $\Delta G_{\text{H}} > 0$ ($\Delta G_{\text{H-positive}}$, weak H adsorption), hydrogen spillover phenomenon occurs from the surface with $\Delta G_{\text{H-negative}}$ to the surface with $\Delta G_{\text{H-positive}}$.^[56] As shown in Figure 5b, Gibbs free energy diagrams display that the first protonation process of HER occurred spontaneously on Mo-SAs, while for Fe-SAs, it is nonspontaneous, indicating that the ability of H atoms to bind to Mo is stronger than Fe.^[57] Therefore, the H intermediate on the Mo sites migrates to the Fe sites through spillover, assists the N_2 hydrogenation on the Fe sites, and synergistically enhances the NRR activity. As shown in Figure 5c,d and Figure S28 (Supporting Information), the charge density difference calculations show that more electrons can be donated to the $^*\text{N}_2$ species from Fe sites than from Mo sites. The Fe atoms in the FeMoPPc system have an increase of +0.12 |e| electrons compared to the FePPc system, while +0.07 |e| electrons are added for the Mo atoms in the FeMoPPc system compared to the MoPPc system. When the number of electrons on the metal site increases, the number of charges flowing to the $\text{N}\equiv\text{N}$ bond to form the M–N bond increases, which is more conducive to the adsorption and activation of N_2 .^[58] It indicates that the adsorption and activation of N_2 by Fe sites are enhanced after adding metal Mo.

3. Conclusion

In summary, a h-SA NRR electrocatalyst with FeN_4 and MoN_4 coordination coanchored to polyphthalocyanine organic framework (POF) by low-temperature melt polymerization, which demonstrated that the Fe-SAs and Mo-SAs active sites synergistically promote the NRR process. uncover that the spin-state formation of 3d orbitals in transition metal ions. Importantly, both experiments and DFT calculations revealed that the addition of Mo-SAs can induce electrons to accumulate on Fe, which was more conducive to the adsorption of N_2 . As a result, Fe changed from high spin to medium spin with a decrease of unpaired electrons, which

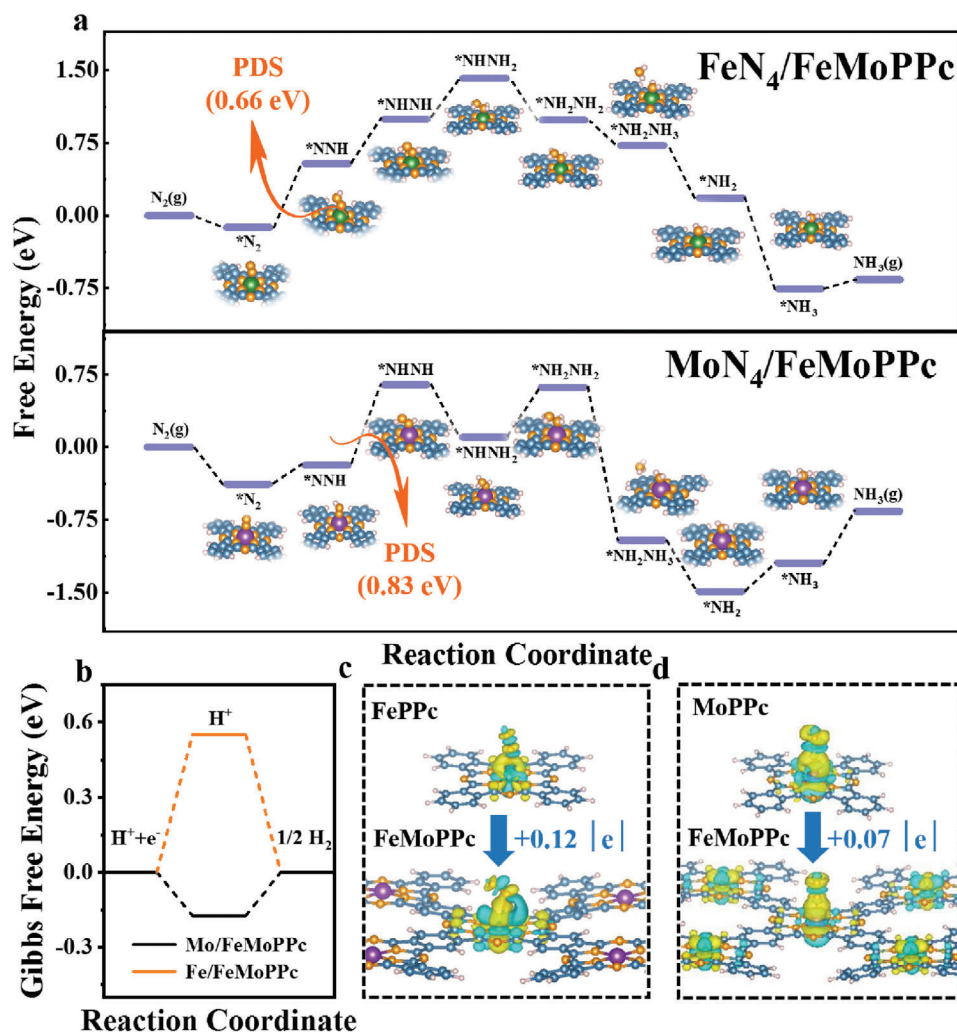


Figure 5. DFT calculations of the NRR activity on FeMoPPc catalysts. a) Different free-energy diagrams for the NRR on Fe atoms of FeMoPPc and Mo atoms of FeMoPPc. b) Different free-energy diagrams for the HER on Fe atoms of FeMoPPc and Mo atoms of FeMoPPc. c) The charge density differences calculations of N₂ bonded to Fe atoms of FePPc and FeMoPPc (the electron excess area and electron deficiency area are represented by yellow and blue-green, respectively). d) The charge density differences calculations of the N₂ bonded to Mo atoms of MoPPc and FeMoPPc.

better coincided with *N₂ unpaired electrons, thereby promoting the first hydrogenation process. Thereby, FeMoPPc exhibits 2.0 and 9.0 times higher Faradaic efficiency and 2.0 and 17.2 times higher NH₃ yields for NRR than FePPc and MoPPc, respectively. This work potentially provides a rational design principle for optimizing noble-metal-free NRR electrocatalysts by smartly altering the specific local environment.

Supporting Information

Supporting Information is available from the Wiley Online Library or from the author.

Acknowledgements

This work was financially supported by the National Natural Science Foundation of China (Nos. 21875221, 22025208, 22075300), the Youth Talent

Support Program of High-Level Talents Special Support Plan in Henan Province (ZYQR201810148), and Creative talents in the Education Department of Henan Province (19HASTIT039). The XAS measurements were performed at the SXRMB and Bio-XAS beamlines at the Canadian Light Source. The authors thank the staff at the BL14W1 beamline of the Shanghai Synchrotron Radiation Facilities for assistance with the EXAFS and XANES measurements.

Conflict of Interest

The authors declare no conflict of interest.

Author Contributions

Z.J.N. conceived the project and idea. W.Y.J. performed the materials preparation, characterization, performance testing, and wrote the article. H.Y.F. performed NEXFAS experiments and data fitting with the discussion with Z.J.N. C.W.Z., Y.G.G., L.J.L., X.H.C., G.K., L.M.L., Z.S.Y., Q.G., L.B.A., and H.J.S. assisted in the materials preparation and data analysis. Y.P.F. performed the theoretical calculations. Z.J.N. supervised the project.

Data Availability Statement

Research data are not shared.

Keywords

charge accumulation, electron spin state, nitrogen reduction reaction, single atom catalysts

Received: July 6, 2021

Revised: August 12, 2021

Published online: September 2, 2021

- [1] R. F. Service, *Science* **2014**, *345*, 610.
- [2] L. Li, C. Tang, X. Cui, Y. Zheng, X. Wang, H. Xu, S. Zhang, T. Shao, K. Davey, S. Qiao, *Angew. Chem., Int. Ed.* **2021**, *60*, 14131.
- [3] S. Liu, T. Qian, M. Wang, H. Ji, X. Shen, C. Wang, C. Yan, *Nat. Catal.* **2021**, *4*, 322.
- [4] T. Wu, H. Zhao, X. Zhu, Z. Xing, Q. Liu, T. Liu, S. Gao, S. Lu, G. Chen, A. M. Asiri, Y. Zhang, X. Sun, *Adv. Mater.* **2020**, *32*, 2000299.
- [5] R. Schlögl, *Angew. Chem., Int. Ed.* **2003**, *115*, 2050.
- [6] Z. Han, C. Choi, S. Hong, T.-S. Wu, Y.-L. Soo, Y. Jung, J. Qiu, Z. Sun, *Appl. Catal., B* **2019**, *257*, 117896.
- [7] J. Guo, C. Y. Lin, Z. Xia, Z. Xiang, *Angew. Chem., Int. Ed.* **2018**, *57*, 12567.
- [8] N. Han, Y. Wang, L. Ma, J. Wen, J. Li, H. Zheng, K. Nie, X. Wang, F. Zhao, Y. Li, J. Fan, J. Zhong, T. Wu, D. J. Miller, J. Lu, S.-T. Lee, Y. Li, *Chem* **2017**, *3*, 652.
- [9] W. Guo, K. Zhang, Z. Liang, R. Zou, Q. Xu, *Chem. Soc. Rev.* **2019**, *48*, 5658.
- [10] Y. Luo, G.-F. Chen, L. Ding, X. Chen, L.-X. Ding, H. Wang, *Joule* **2019**, *3*, 279.
- [11] S. Z. Andersen, M. J. Statt, V. J. Bukas, S. G. Shapel, J. B. Pedersen, K. Krempel, M. Saccoccio, D. Chakraborty, J. Kibsgaard, P. C. K. Vesborg, J. Nørskov, I. Chorkendorff, *Energy Environ. Sci.* **2020**, *13*, 4291.
- [12] J. Deng, J. A. Iñiguez, C. Liu, *Joule* **2018**, *2*, 846.
- [13] K. Han, J. Luo, Y. Feng, L. Xu, W. Tang, Z. L. Wang, *Energy Environ. Sci.* **2020**, *13*, 2450.
- [14] Y. Ren, C. Yu, X. Tan, H. Huang, Q. Wei, J. Qiu, *Energy Environ. Sci.* **2021**, *14*, 1176.
- [15] M. Kitano, Y. Inoue, Y. Yamazaki, F. Hayashi, S. Kanbara, S. Matsuishi, T. Yokoyama, S. W. Kim, M. Hara, H. Hosono, *Nat. Chem.* **2012**, *4*, 934.
- [16] V. Kyriakou, I. Garagounis, E. Vasileiou, A. Vourros, M. Stoukides, *Catal. Today* **2017**, *286*, 2.
- [17] C. Tang, S. Z. Qiao, *Chem. Soc. Rev.* **2019**, *48*, 3166.
- [18] S. Z. Andersen, V. Colic, S. Yang, J. A. Schwalbe, A. C. Nielander, J. M. McEnaney, K. Enemark-Rasmussen, J. G. Baker, A. R. Singh, B. A. Rohr, M. J. Statt, S. J. Blair, S. Mezzavilla, J. Kibsgaard, P. C. K. Vesborg, M. Cargnello, S. F. Bent, T. F. Jaramillo, I. E. L. Stephens, J. K. Nørskov, I. Chorkendorff, *Nature* **2019**, *570*, 504.
- [19] B. Yang, W. Ding, H. Zhang, S. Zhang, *Energy Environ. Sci.* **2021**, *14*, 672.
- [20] N. Cao, G. Zheng, *Nano Res.* **2018**, *11*, 2992.
- [21] H. K. Chae, D. Y. Siberio-Perez, J. Kim, Y. Go, M. Eddaoudi, A. J. Matzger, M. O'Keefe, O. M. Yaghi, *Nature* **2004**, *427*, 523.
- [22] Y.-C. Hao, Y. Guo, L.-W. Chen, M. Shu, X.-Y. Wang, T.-A. Bu, W.-Y. Gao, N. Zhang, X. Su, X. Feng, J.-W. Zhou, B. Wang, C.-W. Hu, A.-X. Yin, R. Si, Y.-W. Zhang, C.-H. Yan, *Nat. Catal.* **2019**, *2*, 448.
- [23] M. Falcone, L. Barluzzi, J. Andrez, F. Fadaei Tirani, I. Zivkovic, A. Fabrizio, C. Corminboeuf, K. Severin, M. Mazzanti, *Nat. Chem.* **2019**, *11*, 154.
- [24] Y. X. Lin, S. N. Zhang, Z. H. Xue, J. J. Zhang, H. Su, T. J. Zhao, G. Y. Zhai, X. H. Li, M. Antonietti, J. S. Chen, *Nat. Commun.* **2019**, *10*, 4380.
- [25] Y. Ma, T. Yang, H. Zou, W. Zang, Z. Kou, L. Mao, Y. Feng, L. Shen, S. J. Pennycook, L. Duan, X. Li, J. Wang, *Adv. Mater.* **2020**, *32*, 2002177.
- [26] Z. H. Xue, S. N. Zhang, Y. X. Lin, H. Su, G. Y. Zhai, J. T. Han, Q. Y. Yu, X. H. Li, M. Antonietti, J. S. Chen, *J. Am. Chem. Soc.* **2019**, *141*, 14976.
- [27] T. Wu, X. Zhu, Z. Xing, S. Mou, C. Li, Y. Qiao, Q. Liu, Y. Luo, X. Shi, Y. Zhang, X. Sun, *Angew. Chem., Int. Ed.* **2019**, *58*, 18449.
- [28] Y. Yang, L. Zhang, Z. Hu, Y. Zheng, C. Tang, P. Chen, R. Wang, K. Qiu, J. Mao, T. Ling, S. Z. Qiao, *Angew. Chem., Int. Ed.* **2020**, *59*, 4525.
- [29] L. Han, X. Liu, J. Chen, R. Lin, H. Liu, F. Lu, S. Bak, Z. Liang, S. Zhao, E. Stavitski, J. Luo, R. R. Adzic, H. L. Xin, *Angew. Chem., Int. Ed.* **2019**, *58*, 2321.
- [30] J. Yao, J. Yan, *Chem* **2020**, *6*, 808.
- [31] S. Ji, Y. Chen, X. Wang, Z. Zhang, D. Wang, Y. Li, *Chem. Rev.* **2020**, *120*, 11900.
- [32] H. Tao, C. Choi, L.-X. Ding, Z. Jiang, Z. Han, M. Jia, Q. Fan, Y. Gao, H. Wang, A. W. Robertson, S. Hong, Y. Jung, S. Liu, Z. Sun, *Chem* **2019**, *5*, 204.
- [33] L. Hu, A. Khaniya, J. Wang, G. Chen, W. E. Kaden, X. Feng, *ACS Catal.* **2018**, *8*, 9312.
- [34] G. Qing, R. Ghazfar, S. T. Jackowski, F. Habibzadeh, M. M. Ashtiani, C. P. Chen, M. R. Smith II, T. W. Hamann, *Chem. Rev.* **2020**, *120*, 5437.
- [35] H. Su, L. Chen, Y. Chen, R. Si, Y. Wu, X. Wu, Z. Geng, W. Zhang, J. Zeng, *Angew. Chem., Int. Ed.* **2020**, *59*, 20411.
- [36] J. Li, S. Chen, F. Quan, G. Zhan, F. Jia, Z. Ai, L. Zhang, *Chem* **2020**, *6*, 885.
- [37] Z. Zhu, H. Yin, Y. Wang, C. H. Chuang, L. Xing, M. Dong, Y. R. Lu, G. Casillas-Garcia, Y. Zheng, S. Chen, Y. Dou, P. Liu, Q. Cheng, H. Zhao, *Adv. Mater.* **2020**, *32*, 2004670.
- [38] G. Yang, J. Zhu, P. Yuan, Y. Hu, G. Qu, B. A. Lu, X. Xue, H. Yin, W. Cheng, J. Cheng, W. Xu, J. Li, J. Hu, S. Mu, J. N. Zhang, *Nat. Commun.* **2021**, *12*, 1734.
- [39] H. Li, J. Wang, R. Qi, Y. Hu, J. Zhang, H. Zhao, J. Zhang, Y. Zhao, *Appl. Catal., B* **2021**, *285*, 119778.
- [40] Z. Li, Z. Zhuang, F. Lv, H. Zhu, L. Zhou, M. Luo, J. Zhu, Z. Lang, S. Feng, W. Chen, L. Mai, S. Guo, *Adv. Mater.* **2018**, *30*, 1803220.
- [41] Y. Pan, S. Liu, K. Sun, X. Chen, B. Wang, K. Wu, X. Cao, W. C. Cheong, R. Shen, A. Han, Z. Chen, L. Zheng, J. Luo, Y. Lin, Y. Liu, D. Wang, Q. Peng, Q. Zhang, C. Chen, Y. Li, *Angew. Chem., Int. Ed.* **2018**, *57*, 8614.
- [42] J. Chen, K. Zou, P. Ding, J. Deng, C. Zha, Y. Hu, X. Zhao, J. Wu, J. Fan, Y. Li, *Adv. Mater.* **2019**, *31*, 1805484.
- [43] S. Yang, Y. Yu, M. Dou, Z. Zhang, F. Wang, *J. Am. Chem. Soc.* **2020**, *142*, 17524.
- [44] H. Cheng, P. Cui, F. Wang, L. X. Ding, H. Wang, *Angew. Chem., Int. Ed.* **2019**, *58*, 15541.
- [45] Y. Guo, Z. Yao, B. J. J. Timmer, X. Sheng, L. Fan, Y. Li, F. Zhang, L. Sun, *Nano Energy* **2019**, *62*, 282.
- [46] G. Chen, P. Liu, Z. Liao, F. Sun, Y. He, H. Zhong, T. Zhang, E. Zschech, M. Chen, G. Wu, J. Zhang, X. Feng, *Adv. Mater.* **2020**, *32*, 1907399.
- [47] Y. Chen, S. Ji, S. Zhao, W. Chen, J. Dong, W. C. Cheong, R. Shen, X. Wen, L. Zheng, A. I. Rykov, S. Cai, H. Tang, Z. Zhuang, C. Chen, Q. Peng, D. Wang, Y. Li, *Nat. Commun.* **2018**, *9*, 5422.
- [48] W. Liu, L. Zhang, X. Liu, X. Liu, X. Yang, S. Miao, W. Wang, A. Wang, T. Zhang, *J. Am. Chem. Soc.* **2017**, *139*, 10790.
- [49] G. B.-C. Marc-André Légaré, R. D. Dewhurst, E. Welz, I. Krummenacher, B. Engels, H. Braunschweig, *Science* **2018**, *359*, 896.

- [50] C. Ling, X. Niu, Q. Li, A. Du, J. Wang, *J. Am. Chem. Soc.* **2018**, *140*, 14161.
- [51] G. Shen, R. Zhang, L. Pan, F. Hou, Y. Zhao, Z. Shen, W. Mi, C. Shi, Q. Wang, X. Zhang, J. J. Zou, *Angew. Chem., Int. Ed.* **2020**, *59*, 2313.
- [52] Y. Sun, S. Sun, H. Yang, S. Xi, J. Gracia, Z. J. Xu, *Adv. Mater.* **2020**, *32*, 2003297.
- [53] Z.-F. Huang, J. Song, Y. Du, S. Xi, S. Dou, J. M. V. Nsanzimana, C. Wang, Z. J. Xu, X. Wang, *Nat. Energy* **2019**, *4*, 329.
- [54] C. He, Z.-Y. Wu, L. Zhao, M. Ming, Y. Zhang, Y. Yi, J.-S. Hu, *ACS Catal.* **2019**, *9*, 7311.
- [55] X. Wang, Y. Zhang, H. Si, Q. Zhang, J. Wu, L. Gao, X. Wei, Y. Sun, Q. Liao, Z. Zhang, K. Ammarah, L. Gu, Z. Kang, Y. Zhang, *J. Am. Chem. Soc.* **2020**, *142*, 4298.
- [56] J. Li, H.-X. Liu, W. Gou, M. Zhang, Z. Xia, S. Zhang, C.-R. Chang, Y. Ma, Y. Qu, *Energy Environ. Sci.* **2019**, *12*, 2298.
- [57] C. Mao, J. Wang, Y. Zou, G. Qi, J. Y. Yang Loh, T. Zhang, M. Xia, J. Xu, F. Deng, M. Ghousoub, N. P. Kherani, L. Wang, H. Shang, M. Li, J. Li, X. Liu, Z. Ai, G. A. Ozin, J. Zhao, L. Zhang, *J. Am. Chem. Soc.* **2020**, *142*, 17403.
- [58] W. Peng, M. Luo, X. Xu, K. Jiang, M. Peng, D. Chen, T. S. Chan, Y. Tan, *Adv. Energy Mater.* **2020**, *10*, 2001364.